



Research Article

Probing Molecular Frame Wigner Time Delay and Electron Wavepacket Phase Structure of CO Molecule

Zhenning Guo ¹, Peipei Ge,¹ Yiqi Fang,¹ Yankun Dou,¹ Xiaoyang Yu,¹ Jiguo Wang,¹ Qihuang Gong,^{1,2,3} and Yunquan Liu ^{1,2,3}

¹State Key Laboratory for Mesoscopic Physics and Frontiers Science Center for Nano-Optoelectronics, School of Physics, Peking University, Beijing 100871, China

²Collaborative Innovation Center of Quantum Matter, Beijing 100871, China

³Collaborative Innovation Center of Extreme Optics, Shanxi University, Taiyuan, Shanxi 030006, China

Correspondence should be addressed to Yunquan Liu; yunquan.liu@pku.edu.cn

Received 1 March 2022; Accepted 6 May 2022; Published 26 May 2022

Copyright © 2022 Zhenning Guo et al. Exclusive Licensee Xi'an Institute of Optics and Precision Mechanics. Distributed under a Creative Commons Attribution License (CC BY 4.0).

The time delay of photoelectron emission serves as a fundamental building block to understand the ultrafast electron emission dynamics in strong-field physics. Here, we study the photoelectron angular streaking of CO molecules by using two-color (400 + 800 nm) corotating circularly polarized fields. By coincidentally measuring photoelectrons with the dissociative ions, we present molecular frame photoelectron angular distributions with respect to the instantaneous driving electric field signatures. We develop a semiclassical nonadiabatic molecular quantum-trajectory Monte Carlo (MO-QTMC) model that fully captures the experimental observations and further *ab initio* simulations. We disentangle the orientation-resolved contribution of the anisotropic ionic potential and the molecular orbital structure on the measured photoelectron angular distributions. Furthermore, by analyzing the photoelectron interference patterns, we extract the sub-Coulomb-barrier phase distribution of the photoelectron wavepacket and reconstruct the orientation- and energy-resolved Wigner time delay in the molecular frame. Holographic angular streaking with bicircular fields can be used for probing polyatomic molecules in the future.

1. Introduction

The photoelectric effect [1], one of the most fundamental light-matter interactions, has been widely used for probing ultrafast dynamics in atoms, molecules, and condensed matter. It has been the spotlight of research in the community of ultrafast and strong-field science. Nowadays, the basic questions about how long the photoionization process takes place and how to identify the specific mechanisms responsible for the measured time delays have been reignited with the emergence of attosecond metrology [2–6]. The concept of the Wigner time delay has been constructed to characterize such photoemission delay [7–9]. To date, most investigations related to time delay were focused on one- or few-photon ionization and strong-field tunneling from atoms or molecules. However, disentangling the time-resolved photoionization dynamics in strong-field multiphoton ionization is still challenging because of complex multipath interferences [10–15].

Recently, the attosecond holographic angular streaking scheme using two-color bicircular fields ($\omega + 2\omega$) has been widely used to explore time-resolved photoemission dynamics in atomic multiphoton ionization [16–21], such as probing the phase and amplitude of emitting wave packets [16], and measuring the time delay of spin-orbit coupled electronic states [20]. In contrast to atomic photoionization, molecular frame measurements of complex molecules show that the spatial distribution of molecular orbitals can result in the displacement of rescattering wavepacket [22], orientation-dependent electron phase distribution [23], and modulation of the releasing time of photoelectrons [24, 25]. Due to the anisotropy of the long-range ionic potential in molecules, the photoelectron interference patterns are distorted. The photoemission has nontrivial spatiotemporal features for complex molecules [26]. In this sense, revealing the time delay of molecular strong-field ionization and clocking the multiphoton ionization of asymmetrical molecules are certainly interesting and would be important in

revealing further fundamental principles in ultrafast physical and chemical sciences.

Here, we employ the phase-locked two-color bicircular (800 nm + 400 nm) fields to investigate the orientation-dependent photoelectron angular streaking of asymmetric CO molecules and to extract the molecular frame sub-Coulomb-barrier phase of the photoelectron wavepacket, which is associated with the molecular Wigner time delay. We measure the molecular frame photoelectron angular distributions of CO molecules in a high-intensity 400 nm circular field and a same-helicity low-intensity 800 nm circular field. The measured photoelectron angular distribution reveals an alternating half-ring pattern, which exhibits a drastic dependence on the molecular orientation angle. We develop a semiclassical nonadiabatic molecular quantum trajectory Monte Carlo (MO-QTMC) model to extract the contribution of the anisotropic Coulomb interaction and the molecular orbital structure from the photoelectron interference patterns. The effect of the sub-Coulomb-barrier phase of emitted electron wavepacket on the photoelectron interference structure has been also revealed. This molecular frame sub-Coulomb-barrier phase depends on the molecular orientation and photoelectron energy, and it is intrinsically related with the Wigner time delay.

2. Materials and Methods

2.1. Experimental Methods. Experimentally, the fundamental field is produced by a femtosecond Ti: sapphire laser amplifier system (25 fs FWHM, 800 nm, and 3 kHz). The second harmonic pulse at 400 nm is generated by using a 250 μm BBO crystal. The two-color bicircular (corotating two-color circularly polarized (CoRTC)) field is realized by using a Mach-Zehnder interferometer scheme. A pair of fused silica wedges are used to precisely adjust the relative phase between the two laser pulses with a time accuracy of ~ 5 as. Three-dimensional momentum vectors of the photoelectrons and fragment ions are coincidentally detected using the cold target recoil ion momentum spectroscopy (COLTRIMS) apparatus [27]. The laser intensities of the 400 nm and 800 nm circular fields are calibrated to be $\sim 8.9 \times 10^{13}$ W/cm² and $\sim 6.3 \times 10^{11}$ W/cm² in our experiment, respectively. In the experiment, the Keldysh parameter is calculated to be $\gamma_{\text{keldysh}} = \sqrt{I_p/2U_p} \sim 3.2$ (I_p is the ionization potential of CO; $U_p = E_0^2/4\omega^2$ is the pondermotive potential with the laser field amplitude E_0 and frequency ω), which is well in multiphoton ionization regime.

We illustrate the principle of probing molecular frame time-resolved electron dynamics via the bicircular field attoclock scheme in Figure 1. The bound electron escapes the molecular potential into different directions by absorbing photons. The resulting parent ion CO⁺ can be populated into the repulsive states by the laser-induced coupling and dissociate into C⁺ and O ions [28]. Within the axial recoil approximation [29, 30], the direction of the ionic fragments' momenta is in accordance with the molecular orientation at the ionization instant. Thus, we can reconstruct the photoelectron momentum distributions in the molecular frame

with the emission direction of C⁺ ions θ_{ion} (see Figure 1 for the definition of the angles) on the polarization plane for the dissociative ionization channel CO⁺ \rightarrow C⁺ + O.

2.2. TDSE Calculation. We solve the two-dimensional TDSE within the Born-Oppenheimer approximation, by writing (in atomic units) [31].

$$i \frac{\partial}{\partial t} \Psi(\mathbf{r}, t) = \left[-\frac{\nabla^2}{2} + V(\mathbf{r}) + \mathbf{r} \cdot \mathbf{E}(t) \right] \Psi(\mathbf{r}, t), \quad (1)$$

where $\Psi(\mathbf{r}, t)$ is the electron wave function and $\mathbf{r} = (x, y)$ is the electron position in the polarization plane of light. Within the single-active-electron (SAE) approximation, the potential in equation (1) is expressed as

$$V(\mathbf{r}) = - \sum_{J=C,O} \frac{Z_J^0 + (Z_J^0 - Z_J^\infty) \exp(-|\mathbf{r} - \mathbf{R}_J|^2/\sigma_J^2)}{\sqrt{|\mathbf{r} - \mathbf{R}_J|^2 + a_J^2}} \dots \quad (2)$$

Here, J labels the carbon and oxygen atom centers located at fixed positions \mathbf{R}_J . Z_J^0 and Z_J^∞ are the bare charge and effective charge of the nucleus J , respectively. The value of Z_J^∞ is derived from a Mulliken analysis of the parent ion. Parameters a_J and σ_J are optimized such that the calculated orbital energy approaches the experimental energy value.

The wave function is propagated using the splitting-operator method [32]. The initial wave function is prepared by the imaginary time propagation. And the real-time evolution of the electron wave function is separated into the bound wave packet and ionizing wave packet at each time step. Then, we project the ionizing wavepacket on the Volkov Hamiltonian and propagate it to the end of the simulation. At last, the final photoelectron momentum distribution is obtained by summing up the ionizing wave packets in momentum space from each time step.

For CO molecule, we consider the 5 σ highest occupied molecular orbital (HOMO). Lower molecular orbitals are not considered here because of their much higher ionization energies (the ionization energies for HOMO and HOMO-1 are 13.9 and 14.9 eV). In Supplementary Figure 1, we display the HOMO wave function of CO in the coordinate space by solving the TDSE. The spatial wave function shows an excellent agreement with the result presented in Ref. [33] which is calculated using the standard software from the quantum chemistry.

2.3. Nonadiabatic MO-QTMC Model. We have also utilized a semiclassical nonadiabatic MO-QTMC [34, 35] model to track the time-resolved ionization dynamics of CO molecules. In this model, we consider the construction of the CO molecular orbital on the carbon and oxygen atom centers, as the linear combination of atomic orbitals (LCAO)

$$\Psi_{\text{co}}(\mathbf{r}) = \sum_{J=C,O} \sum_a c_{Ja} \psi_a(\mathbf{r} - \mathbf{R}_J). \quad (3)$$

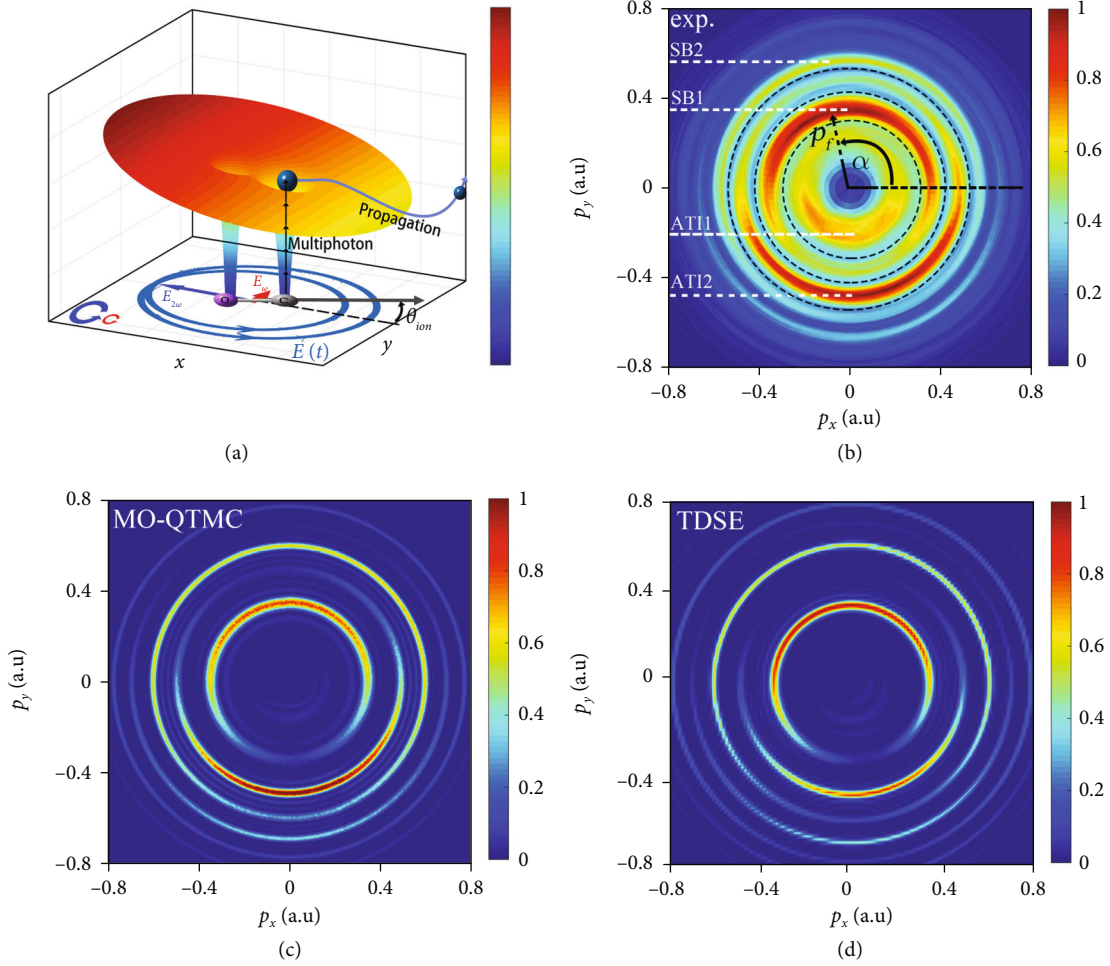


FIGURE 1: Holographic angular streaking scheme and photoelectron momentum distributions. (a) Schematic diagram of the bicircular scheme for measuring the time-resolved electron dynamics of asymmetrical CO molecule. The synthesized electric field $E(t)$ is composed of the phase-locked strong 400 nm and the weak 800 nm circular field. The bound electron wavepacket is promoted into the continuum through multiphoton ionization. The gray thin arrow indicates the emission direction of the C^+ ions for the dissociative CO molecules. (b) The measured photoelectron momentum distribution. The positions of ATI and SB are marked, respectively. (c, d) The simulated photoelectron momentum distribution using the nonadiabatic MO-QTMC model and TDSE, respectively.

The $\mathbf{r} - \mathbf{R}_j$ labels the nuclei located at fixed positions \mathbf{R}_j . For the HOMO of CO, the expand coefficients c_{ja} and atomic orbitals ψ_a are tabulated in Refs. [36, 37]. As seen in Ref. [37], one can find that the molecular orbital at the carbon (oxygen) atom side is approximated by the atomic 2s and 3s (2s and 2p) orbits. Additionally, the HOMO wave function of CO exhibits an evident bias towards the carbon atom side (see Supplementary Figure 1). This results in a higher ionization rate from the carbon sides. This implies that the liberated photoelectron mainly originates from the carbon atom side. Since the inclusion of all superimposed atomic orbitals will introduce a great complexity and huge computation, we use the bonding superposition of two s atomic orbitals to mimic the HOMO of CO in the semiclassical nonadiabatic MO-QTMC model. This simplified approximation has been considered for N_2 and works well in reproducing the experimental measurement [23]. In this case, the HOMO

wave function of CO in both coordinate (\mathbf{r}) and momentum (\mathbf{k}) representations are

$$\begin{aligned}\Psi_{CO}(\mathbf{r}) &= \frac{1}{\sqrt{2+2S_{OI}}} \left[a\psi_s\left(\frac{\mathbf{r}+\mathbf{R}}{2}\right) + b\psi_s\left(\frac{\mathbf{r}-\mathbf{R}}{2}\right) \right] \\ &= \frac{\kappa^{3/2}}{\sqrt{2\pi(1+S_{OI})}} \left[a \exp\left(-\eta\left|\frac{\mathbf{r}+\mathbf{R}}{2}\right|\right) + b \exp\left(-\eta\left|\frac{\mathbf{r}-\mathbf{R}}{2}\right|\right) \right],\end{aligned}\quad (4)$$

$$\begin{aligned}\Phi_{CO}(\mathbf{k}) &= \left[a\phi_s(\mathbf{k})e^{-i\mathbf{R}\cdot\mathbf{k}/2} + b\phi_s(\mathbf{k})e^{i\mathbf{R}\cdot\mathbf{k}/2} \right] \\ &= \frac{2}{\pi\sqrt{1+S_{OI}}} \frac{\eta^{5/2}}{(k^2+\eta^2)^2} \left[ae^{-i\mathbf{R}\cdot\mathbf{k}/2} + be^{i\mathbf{R}\cdot\mathbf{k}/2} \right].\end{aligned}\quad (5)$$

Here, $\eta = \sqrt{2I_p}$. Parameter a and parameter b are related to the spatial electron density of carbon and oxygen atoms in a CO molecule, respectively. For the HOMO of a CO

molecule, $a = 0.75$ and $b = 0.25$. These two parameters are chosen to match the experimental orientation-dependent ionization rate [38]. In Supplementary Figure 2, we illustrate the orientation-dependent ionization rates of CO by using the nonadiabatic MO-QTMC and TDSE, where 0° corresponds to the electronic field pointing from the carbon atom to the oxygen atom. The results from the nonadiabatic MO-QTMC model and TDSE show excellent agreement, which suggests the validity of the molecular orbital approximation used in nonadiabatic MO-QTMC.

In the next step, we present the details of the solution of saddle-point molecular strong-field approximation [39, 40]. The direct transition matrix element in the length gauge is given as [41]

$$M(\mathbf{p}) = -i \int_0^{T_p} dt \langle \mathbf{p} + \mathbf{A}(t) | \mathbf{r} \cdot \mathbf{E}(t) | \Psi_{\text{CO}}(\mathbf{r}) \rangle e^{iS(t)}. \quad (6)$$

Here, T_p is the pulse turn-off time and \mathbf{p} is the canonical momentum. The ionization energy I_p is 0.51 a.u. $\mathbf{A}(t)$ is the instantaneous vector and $\mathbf{E}(t)$ is the electronic field. $S(t) = \int_0^t d\tau \{ [\mathbf{p} + \mathbf{A}(\tau)]^2 / 2 + I_p \}$ is the classical action. The coordinate space wave function $\Psi_{\text{CO}}(\mathbf{r})$ is given by equation (4). Since the classical action $S(t)$ is an exponent term and it is a rapidly oscillating function of time t , we can use the saddle-point approximation by deforming the contour integral in the complex plane and passing near a saddle point to calculate the integral. The integration over time t is thus recast in the form of a sum over saddle points,

$$M(\mathbf{p}) = \sum_s \left\{ \left(2\sqrt{2\pi} i^{3/2} \ddot{S}^{1/2} e^{iS(t_s)} \right) \times \left\{ e^{-i\mathbf{k} \cdot \mathbf{R}/2} \left(a + b e^{i\mathbf{k} \cdot \mathbf{R}} \right) \right. \right. \\ \times \left[E_x(t_s) k_x \cos \alpha - E_x(t_s) k_y \sin \alpha \right. \\ \left. \left. + E_y(t_s) k_x \sin \alpha + E_y(t_s) k_y \cos \alpha \right] \right\}. \quad (7)$$

From this transition amplitude $M(\mathbf{p})$ in equation (7), we analytically obtain the initial momentum distributions and sub-Coulomb-barrier phase structure of the emitted electron wave packet. We obtain the initial coordinates of photoelectrons with the saddle-point approximation by using the imaginary time theory in the complex plane. Then, we sample the photoelectrons using the Monte Carlo approach and propagate the classical trajectories at the exit with the ‘‘quantum’’ phase in the combined molecular Coulomb potential and electric field of the laser pulse. The photoelectron propagates classically in the laser field and Coulomb field governed by the Newtonian equation

$$\ddot{\mathbf{r}} = V(\mathbf{r}, \mathbf{R}) - \mathbf{E}(t) = -\frac{(\mathbf{r} - \mathbf{R}/2)}{2|\mathbf{r} - \mathbf{R}/2|^3} - \frac{(\mathbf{r} + \mathbf{R}/2)}{2|\mathbf{r} + \mathbf{R}/2|^3} - \mathbf{E}(t). \quad (8)$$

The phase of each classical trajectory for emitted electrons is composed of the sub-barrier phase acquired during the ionization process and the propagation phase accumu-

lated by the classical motion. The detailed description of the nonadiabatic MO-QTMC is given in the supplementary material.

It should be noted that unlike the saddle-point molecular strong-field approximation, in which the long-range Coulomb potential has been ignored, we have included the contribution of long-range Coulomb potential in semiclassical propagation in the nonadiabatic MO-QTMC model. This model can be employed to disentangle the contributions of molecular orbital-corrected ionization rate, sub-Coulomb-barrier phase, and the long-range Coulomb potential and analyze their individual effects in intense-light-molecule interaction.

3. Results and Discussion

In the synthesized CoRTC laser field, the strong 400 nm laser field is used to ionize CO molecules. The introduction of the weak 800 nm laser field breaks the symmetry of original circular 400 nm light field, leading to the sideband (SB) structures between the neighboring 400 nm above-threshold ionization (ATI) peaks. The measured momentum distribution accumulated all orientations of the CO molecular axis with respect to the light’s polarization plane is illustrated in Figure 1(b). Here, α is the most probable emission angle of photoelectrons with respect to the x -direction. It is evident that the momentum pattern is composed of ATI and SB half-rings. These interference rings are modulated as a function of the photoelectron emission angle in the polarization plane.

To visualize the molecular orientation-dependent interference pattern, we illustrate the photoelectron angular distribution as a function of θ_{ion} , as shown in Figures 2(a) and 3(a), which correspond to SB1 and ATI2 peaks, respectively, after normalizing with the photoelectron angular distribution at each C^+ emission angle θ_{ion} . Here, the C^+ emission angle θ_{ion} is selected within a conical cut of $\pm 10^\circ$ out of the polarization $x - y$ plane in the momentum slice with $|p_z| < 0.1$ a.u. (p_z is the electron momentum along the laser propagation direction). For both SB1 and ATI2 peaks, the overall distributions are divided into two tilted strips around $\theta_{\text{ion}} = \sim 60^\circ$ and the emission angle α varies as a function of θ_{ion} in each tilted strip.

To interpret the experiment results, we have solved the TDSE (see Section 2.2) and performed the simulation with the nonadiabatic MO-QTMC model (see Section 2.3). The molecular orientation-integrated photoelectron momentum distributions within the polarization plane for nonadiabatic MO-QTMC and TDSE are shown in Figures 1(c) and 1(d), respectively. The changes of α as a function of θ_{ion} for SB1 and ATI2 peaks with nonadiabatic MO-QTMC are shown in Figures 2(b) and 3(b), respectively. For TDSE, the simulated results for SB1 and ATI2 peaks are displayed in Figures 2(c) and 3(c), respectively. For a quantitative comparison of the two theoretical models and experimental measurements, we have extracted the most probable electron emission angles from the correlation plots (the white lines in Figures 2(b), 2(c), 3(b), and 3(c)). The corresponding results for SB1 and ATI2 peaks are shown in Figures 2(d)

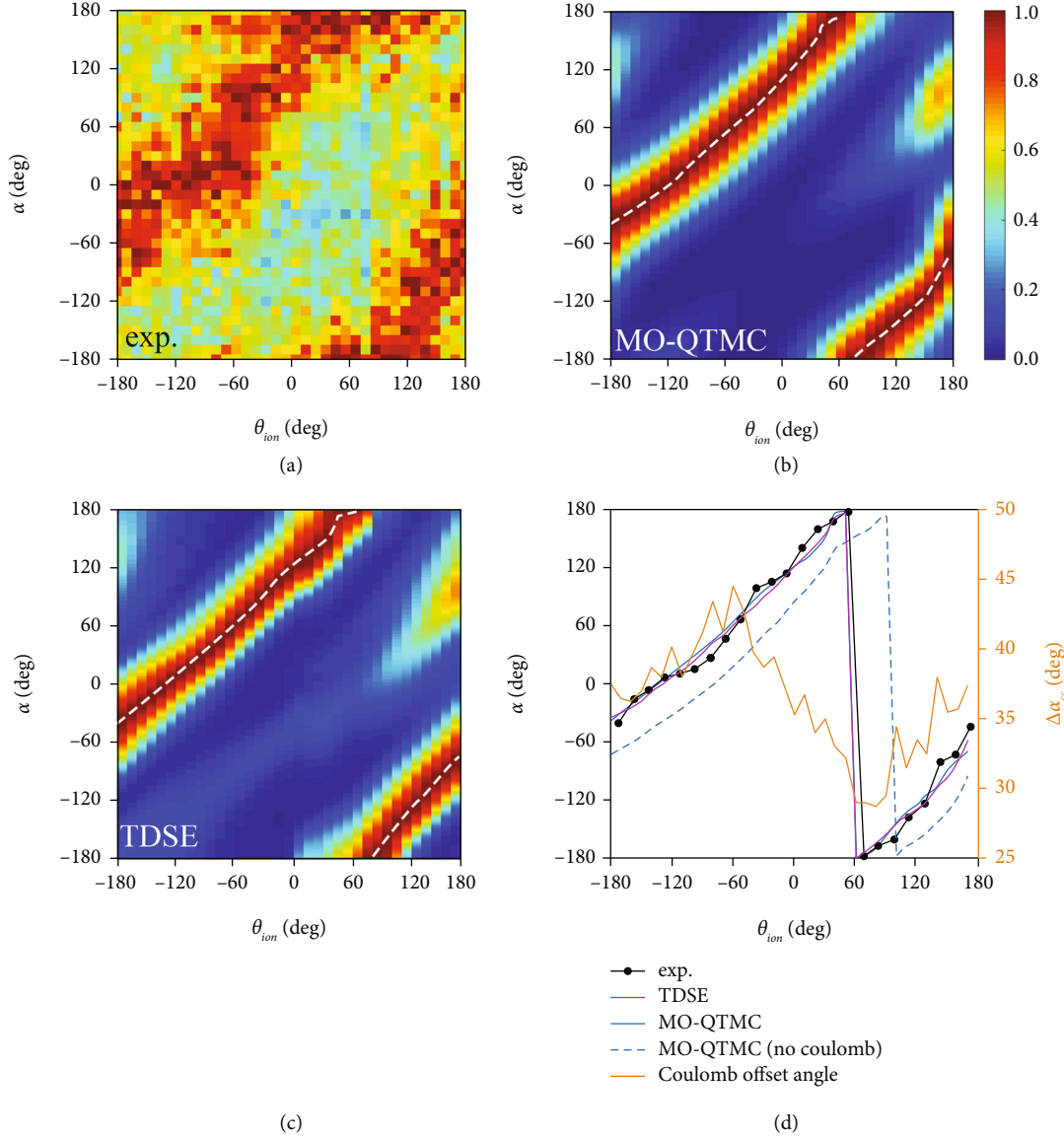


FIGURE 2: Photoelectron angular distribution with respect to the C^+ ion emission angle for SB1 peaks. (a) The measured photoelectron angular distribution as a function of the C^+ ion emission angle θ_{ion} for SB1 peak. Here, the photoelectron angular distributions are obtained by integrating over the radial momentum $p_f = \sqrt{p_x^2 + p_y^2}$ in the range of $\Delta p_f = 0.08$ a.u. centered at the peak of the SB1 position, which is indicated by the black circle in Figure 1(b). (b, c) The simulated result of SB1 peak by the nonadiabatic MO-QTMC and TDSE. The most probable electron emission angle is denoted by the white dotted line. (d) The most probable electron emission angle for SB1 peak from the experiment (the black line), nonadiabatic MO-QTMC model (the blue solid line), and TDSE (the purple line). The blue dashed line is calculated using the nonadiabatic MO-QTMC without the Coulomb interaction after ionization. The orange curve on the right vertical scale indicates the deflected angle because of the Coulomb interaction after ionization.

and 3(d). It is evident that the simulated oscillation of photoelectron angular distributions using the nonadiabatic MO-QTMC and TDSE show excellent agreement with the experiment results.

The most probable emission angle in each interference ring can be given by $\alpha = \Delta\alpha + \alpha_{streak}$. Within strong-field approximation, the streaking angle α_{streak} originates from the vector potential which trails the rotating electric field $\mathbf{E}(t)$ by 90° (SB1: $\alpha_{streak} = 90^\circ$; ATI2: $\alpha_{streak} = -90^\circ$). According

to the nonadiabatic MO-QTMC, the relative shift peak $\Delta\alpha$ is decomposed as the sum of three contributions:

$$\Delta\alpha = \Delta\alpha_{mo} + \Delta\alpha_{ini} + \Delta\alpha_{cc}. \quad (9)$$

The term $\Delta\alpha_{mo}$ results from the product of the molecular orbital structure and the ionization rate for the CoRTC field, which results in a shift of the photoelectron ionization time relative to the electric field peak [26]. Here, the molecular

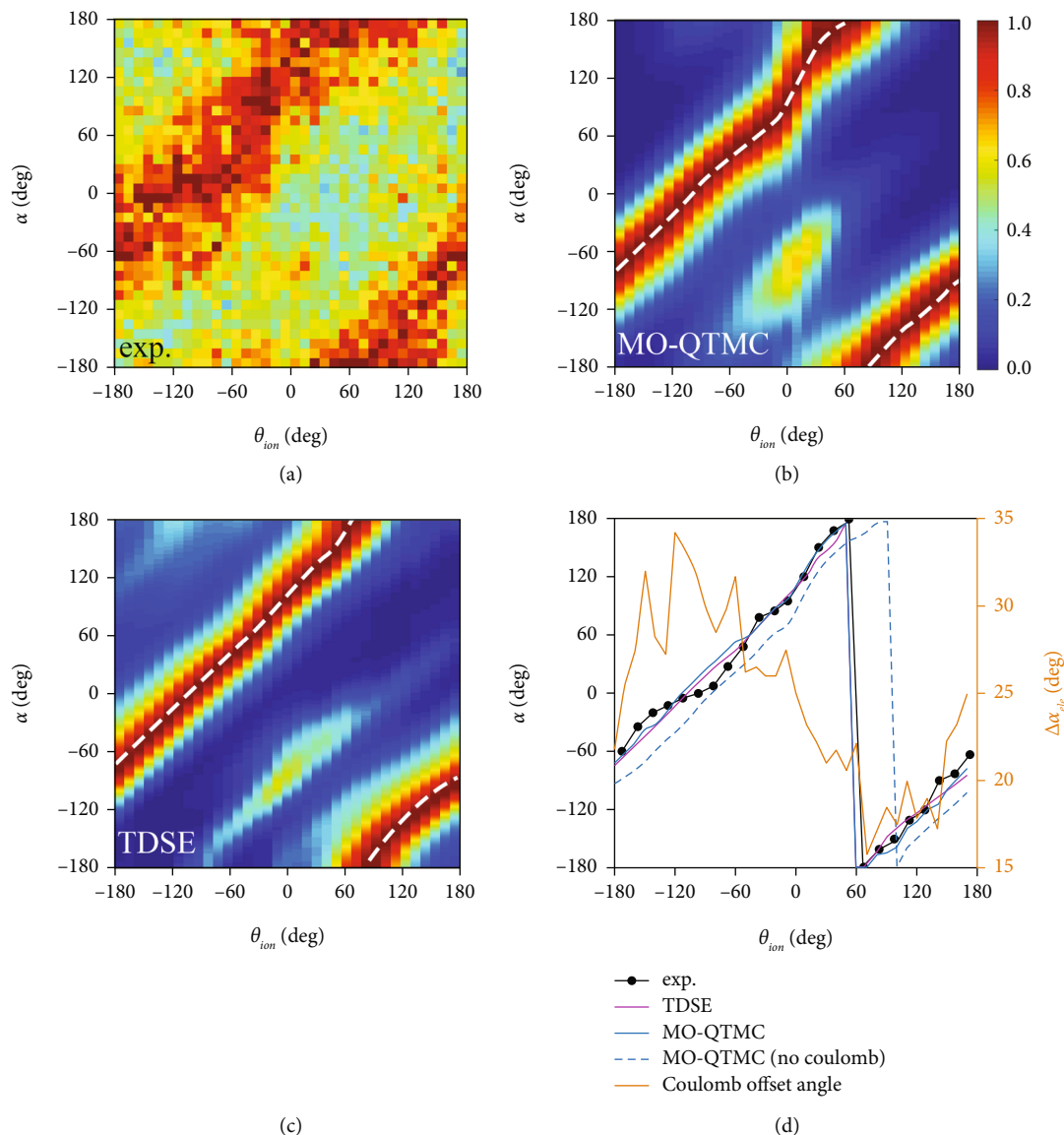


FIGURE 3: Photoelectron angular distribution with respect to the C^+ ion emission angle for ATI2 peaks. (a) Experimental distribution. Here, the photoelectron angular distributions are obtained by integrating over the radial momentum $p_f = \sqrt{p_x^2 + p_y^2}$ in the range of $\Delta p_f = 0.08$ a.u. centered at the peak of the ATI2 position. (b, c) The simulated distributions using nonadiabatic MO-QTMC and TDSE. (d) The extracted most probable electron emission angle for the ATI2 peak from the experiment (the black line), nonadiabatic MO-QTMC model (the blue solid line), and TDSE (the purple line). The blue dashed line is calculated using the nonadiabatic MO-QTMC without the Coulomb interaction after ionization. The orange curve on the right vertical scale indicates the deflected angle because of the Coulomb interaction after ionization.

orbital structure is associated with the anisotropic spatial distribution of electron density in HOMO of the CO molecule. The offset, $\Delta\alpha_{ini}$, results from the accumulated phase term ϕ_{ini} during the sub-Coulomb-barrier ionization process, which is related to the Wigner time delay information for the transition from the bound state to the continuum state [22]. The term $\Delta\alpha_{cc}$ is the angular offset arising from the long-range Coulomb interaction after ionization. One can study these effects using the nonadiabatic MO-QTMC model.

We have calculated the photoelectron angular distributions for different molecular orientations using the nonadiabatic MO-QTMC without the long-range Coulomb potential and then extracted the most probable emission angle for each orientation. The most probable emission angles for SB1 and ATI2 are depicted in Figures 2(d) and 3(d) (blue dashed lines), respectively. Then, we subtract the streaking angle α_{streak} from α and obtain the change $\Delta\alpha$ of the electron emission angle as a function of θ_{ion} (i.e., $\Delta\alpha = \alpha - \alpha_{streak}$ or $\Delta\alpha = \alpha - \alpha_{streak} + 360^\circ$ in the range of $-180^\circ < \theta_{ion} < 100^\circ$ or

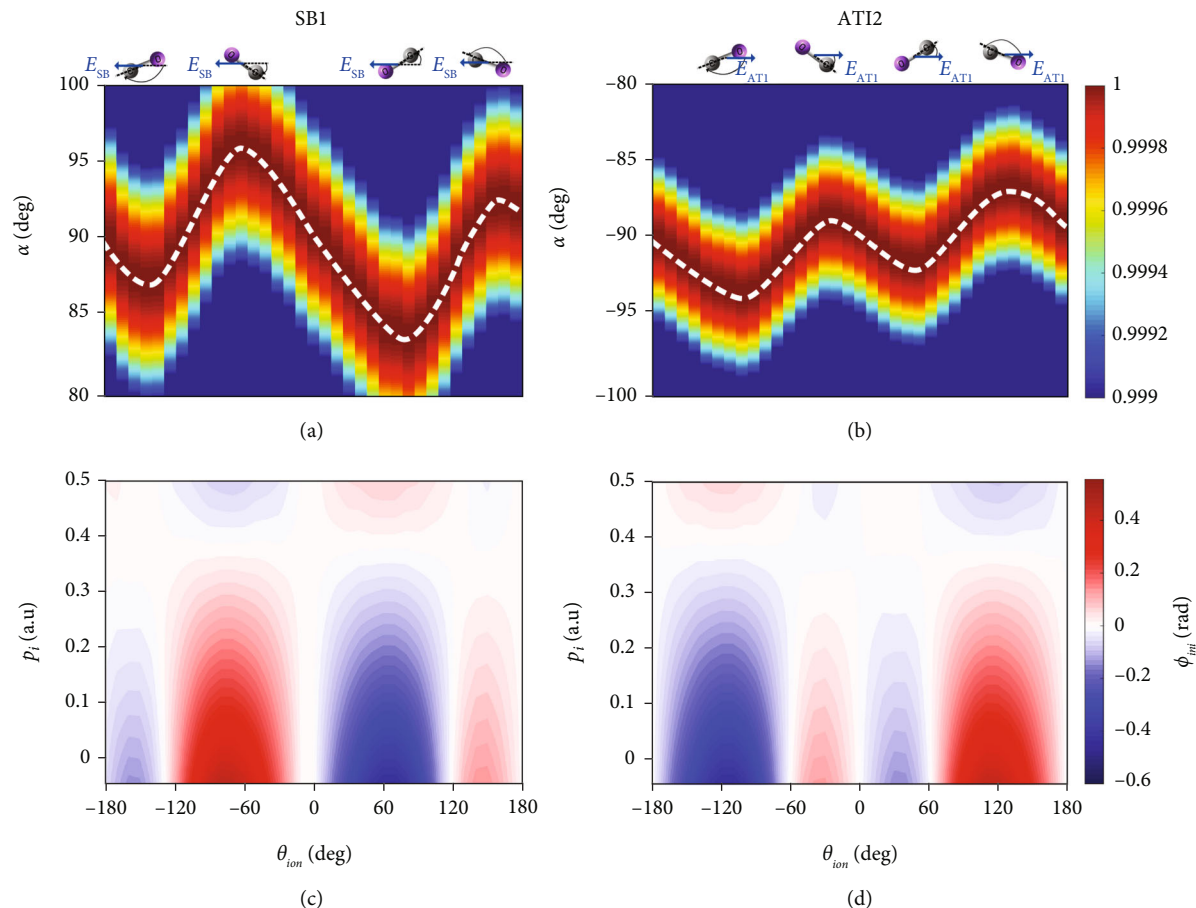


FIGURE 4: Simulated electron emission angle $\Delta\alpha_{\text{ini}} + \alpha_{\text{streak}}$ and the sub-Coulomb-barrier phase in molecular frame. (a, b) Correlation between the electron emission angle and the C^+ ion emission angle because of the sub-Coulomb-barrier phase calculated by the nonadiabatic MO-QTMC, corresponding to the SB1 and ATI2 peaks, respectively. (c, d) The sub-Coulomb-barrier phase ϕ_{ini} as a function of the initial momentum p_i for different C^+ ion emission angles for the SB1 (c) and ATI2 (d) peaks, respectively. The value of ϕ_{ini} is denoted by the linear scale.

$100^\circ < \theta_{\text{ion}} < 180^\circ$). The resulting $\Delta\alpha$ of the SB1 peak (Figure 2(d)) increases from the negative difference of -160° at $\theta_{\text{ion}} = -180^\circ$ to a positive value of 160° at $\theta_{\text{ion}} = 180^\circ$. While for the ATI2 peak (Figure 3(d)), the $\Delta\alpha$ increases from -170° at $\theta_{\text{ion}} = -180^\circ$ to 170° at $\theta_{\text{ion}} = 180^\circ$. Because the contribution of the long-range ionic Coulomb potential has been removed, $\Delta\alpha$ is decomposed as the sum of $\Delta\alpha_{\text{mo}}$ and $\Delta\alpha_{\text{ini}}$ (i.e., $\Delta\alpha = \Delta\alpha_{\text{mo}} + \Delta\alpha_{\text{ini}}$). Notice that $\Delta\alpha_{\text{ini}}$ varies on the order of a few degrees (as seen in Figures 4(a) and 4(b)) and the slight contribution of $\Delta\alpha_{\text{ini}}$ is omitted. In this case, the change of the emission angle only contains the contribution of $\Delta\alpha_{\text{mo}}$ (i.e., $\Delta\alpha = \Delta\alpha_{\text{mo}}$). If neglecting the Coulomb interaction after ionization, the electron emission angle is determined by the vector potential at the release time. One can directly obtain the release-time variation with respect to the laser field peak from the change of the emission angle of photoelectrons [24, 25]. We then obtain the corresponding ionization-time shift $\sim \pm 593$ attosecond (as) for the SB1 peak and $\sim \pm 629$ as for the ATI2 peak with respect to the instant when the CoRTC field maximizes.

After ionization, the motion of the emitted electron is affected by the molecular anisotropic Coulomb potential, resulting in an orientation-dependent angular offset $\Delta\alpha_{\text{cc}}$. The angular offset $\Delta\alpha_{\text{cc}}$ can be obtained by comparing the nonadiabatic MO-QTMC calculations with and without the long-range Coulomb interaction. The corresponding results are depicted with the orange lines (on the right vertical scale) in Figures 2(d) and 3(d). Comparing the angular offset $\Delta\alpha_{\text{cc}}$ of SB1 and ATI2 peaks, one can observe that the angular offset $\Delta\alpha_{\text{cc}}$ of the SB1 peak is larger than that of the ATI2 peak at the same C^+ ion emission angle θ_{ion} . This means that the long-range Coulomb potential would result in a larger angular offset effect for photoelectrons with lower kinetic energy.

The sub-Coulomb-barrier phase of the emitted electron wavepacket will also introduce a nonignorable angular offset. By excluding the effect of the molecular orbital structure and long-range Coulomb potential, we extract the changes of the photoelectron angular distributions for SB1 and ATI2 peaks induced solely by the sub-Coulomb-barrier phase (In this case, $\Delta\alpha_{\text{cc}} = 0^\circ$ and $\Delta\alpha_{\text{mo}} = 0^\circ$). The

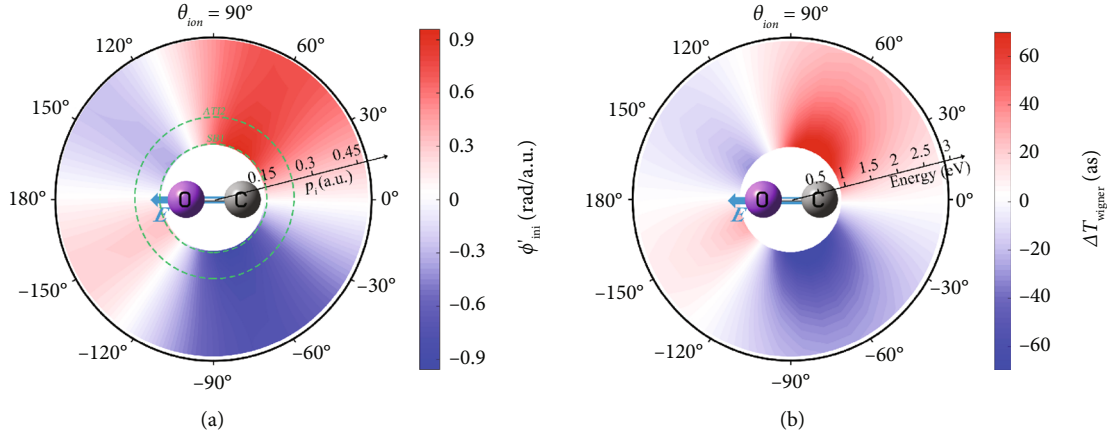


FIGURE 5: Simulated changes of the phase gradient and Wigner time delay in molecular frame. (a) The simulated sub-Coulomb-barrier phase gradient, ϕ'_{ini} , as a function of the initial momentum p_i and the molecular orientation θ_{ion} . The value of ϕ'_{ini} is donated by the color scale. (b) The constructed orientation-dependent Wigner time delay as a function of the electron kinetic energy. The blue arrow represents the direction of laser field $E(t)$ of the most probable electron emission of SB1 peaks.

results of SB1 and ATI2 peaks are depicted in Figures 4(a) and 4(b), respectively. The most probable emission of photoelectrons ($\alpha = \Delta\alpha_{\text{ini}} + \alpha_{\text{streak}}$) is marked by the white dashed line. Both SB1 and ATI2 peaks show the variation of emission angles on the order of a few degrees. Importantly, the overall shape shows the obvious asymmetric oscillation, which includes a large oscillation peak ($\Delta\alpha_{\text{ini}} = \sim \pm 9^\circ / \pm 5.5^\circ$ for SB1/ATI2) and a small oscillation peak ($\Delta\alpha_{\text{ini}} = \sim \pm 4^\circ / \pm 2.5^\circ$ for SB1/ATI2). Furthermore, comparison of the modulation amplitude for SB1 and ATI2 peaks indicates that the change of the electron emission angle $\Delta\alpha_{\text{ini}}$ also depends on the final momentum \mathbf{p}_f . Note that the final momentum is associated with the initial momentum \mathbf{p}_i by $\mathbf{p}_f = \mathbf{p}_i - \mathbf{A}(t)$. Here, the initial momentum \mathbf{p}_i is perpendicular to the instantaneous laser electric field $\mathbf{E}(t)$. This implies that the angular offset $\Delta\alpha_{\text{ini}}$ at a given value of \mathbf{p}_f directly allows us to quantify the angular offset at the corresponding initial momentum \mathbf{p}_i with $\mathbf{p}_i = \mathbf{p}_f + \mathbf{A}(t)$. After excluding the contributions of the molecular orbital and long-range Coulomb potential, we calculate the sub-Coulomb-barrier phase ϕ_{ini} as a function of p_i and the molecular orientation θ_{ion} for SB1 and ATI2 peaks by the nonadiabatic MO-QTMC model, as shown in Figures 4(c) and 4(d), respectively. It is evident that the sub-Coulomb-barrier phase ϕ_{ini} is highly dependent on molecular orientation angle θ_{ion} for both SB1 and ATI2 peaks. And the vanishing sub-Coulomb-barrier phase ϕ_{ini} at about $\theta_{\text{ion}} = 0^\circ$ and $\sim \pm 120^\circ$ ($\theta_{\text{ion}} = 0^\circ$ and $\sim \pm 60^\circ$) for the SB1 (ATI2) peak corresponds to the simultaneous vanishing angular offset $\Delta\alpha_{\text{ini}}$.

The offset angle $\Delta\alpha_{\text{ini}}$ is directly related to the sub-Coulomb-barrier phase gradient ϕ'_{ini} (where $\phi'_{\text{ini}} = \partial\phi_{\text{ini}}/\partial p_i$) [18]. Using the nonadiabatic MO-QTMC model, we extract the sub-Coulomb-barrier phase gradient ϕ'_{ini} as a function of the molecular orientation θ_{ion} and the initial momentum p_i , as shown in Figure 5(a). For the selected values of p_i (the green lines in Figure 5(a)), the oscillation

of the negative sub-Coulomb-barrier phase gradient $-\phi'_{\text{ini}}$ with respect to θ_{ion} closely resembles that of $\Delta\alpha_{\text{ini}}$ with respect to θ_{ion} . And the sub-barrier phase gradient ϕ'_{ini} tends to gradually decrease with the increasing initial momentum p_i , which is consistent with the fact that the SB1 peak (with a smaller initial momentum p_i) shows a larger oscillation amplitude as compared to the ATI2 peak (with a larger initial momentum p_i).

The energy-dependent sub-Coulomb-barrier phase of the emitted electron wavepacket is linked to the Wigner time delay $\Delta\tau_w$ [7, 8], which can be defined as the derivative of the sub-Coulomb-barrier phase of the wavepacket with respect to the energy E , i.e., $\Delta\tau_w = \hbar\partial\phi_{\text{ini}}/\partial E$. Considering the symmetry of the circularly polarized single-color 400 nm field (the probing 800 nm light field is perturbative in CoRTC field), the laser's vector $\mathbf{A}(t)$ is constant and the photoelectron energy E is associated with both the initial momentum and the final momentum by $E = p_f^2/2 = (p_i - |\mathbf{A}(t)|)^2/(2m_e)$ (m_e is the electron's mass). Thus, the Wigner time delay $\Delta\tau_w$ is given by $\Delta\tau_w = (\hbar m_e/p_f) \cdot (\partial\phi_{\text{ini}}(p_i)/\partial p_i) = \hbar m_e \phi'_{\text{ini}}(p_i)/p_f$. Having the orientation-dependent sub-barrier phase gradient ϕ'_{ini} , one can obtain the molecular frame Wigner time delay $\Delta\tau_w$ with respect to different photoelectron energies. Figure 5(b) displays the obtained molecular orientation-dependent Wigner time delays, as a function of the electron energy E . It is evident that the magnitude of $\Delta\tau_w$ decreases when increasing electron energy E . And the Wigner time delay $\Delta\tau_w$ for electrons emitted from the carbon atom side is larger than that of electrons emitted from the oxygen atom side. This high asymmetry of $\Delta\tau_w$ reflects the characteristics of the ionizing orbitals of CO (see Supplementary Figure 1). The observed asymmetric offset angle $\Delta\alpha_{\text{ini}}$ (Figures 4(a) and 4(b)) is a fingerprint of the accumulated phase in sub-Coulomb-barrier process, and it encodes the photoemission time delay for strong-field molecular ionization.

4. Conclusion

In summary, we have measured the molecular frame photoelectron momentum distribution of CO molecules by using two-color bicircular fields. In theory, we have developed a dedicated nonadiabatic MO-QTMC model to disentangle the orientation-dependent behavior of molecular Coulomb interaction and molecular orbital structure on photoelectron angular distributions. Using the bicircular scheme, one is allowed to track the time-resolved ionization dynamics and to reveal the emitted electron wavepacket phase structure and asymmetric Wigner time delay of photoemission in strong-field multiphoton ionization of CO molecules. This work shows the promising potential application in exploring the time-resolved ionization process and measuring structured Wigner time delay of polyatomic molecules [42].

Data Availability

The data that support the plots within this paper and other findings of this study are available from the corresponding author upon reasonable request.

Conflicts of Interest

The authors declare no competing financial interests.

Authors' Contributions

Z. Guo, P. Ge, and Y. Fang performed the experiments. Z. Guo and Y. Liu analyzed and interpreted the data. Simulations were implemented by Z. Guo. This project was coordinated by Y. Liu. All authors discussed the results and wrote the paper.

Acknowledgments

This work is supported by the National Science Foundation of China (Grant Nos. 92050201, 11774013, and 11527901).

Supplementary Materials

Supplementary Figure 1: coordinate space wave function for the 5σ HOMO of CO. Supplementary Figure 2: calculated ionization rates for CO using nonadiabatic MO-QTMC and TDSE models. (*Supplementary Materials*)

References

- [1] A. Einstein, "Über einen die Erzeugung und Verwandlung des Lichtes betreffenden heuristischen Gesichtspunkt," *Annalen der Physik*, vol. 322, no. 6, pp. 132–148, 1905.
- [2] M. Schultze, M. Fieß, N. Karpowicz et al., "Delay in photoemission," *Science*, vol. 328, no. 5986, pp. 1658–1662, 2010.
- [3] J. Vos, L. Cattaneo, S. Patchkovskii et al., "Orientation-dependent stereo Wigner time delay and electron localization in a small molecule," *Science*, vol. 360, no. 6395, pp. 1326–1330, 2018.
- [4] J. Rist, K. Klyssek, N. M. Novikovskiy et al., "Measuring the photoelectron emission delay in the molecular frame," *Nature Communications*, vol. 12, no. 1, p. 6657, 2021.
- [5] S. Beaulieu, A. Comby, A. Clergerie et al., "Attosecond-resolved photoionization of chiral molecules," *Science*, vol. 358, no. 6368, pp. 1288–1294, 2017.
- [6] V. Gruson, L. Barreau, Á. Jiménez-Galan et al., "Attosecond dynamics through a Fano resonance: monitoring the birth of a photoelectron," *Science*, vol. 354, no. 6313, pp. 734–738, 2016.
- [7] E. P. Wigner, "Lower limit for the energy derivative of the scattering phase shift," *Physical Review Journals Archive*, vol. 98, no. 1, pp. 145–147, 1955.
- [8] F. T. Smith, "Lifetime matrix in collision theory," *Physical Review Journals Archive*, vol. 118, no. 1, pp. 349–356, 1960.
- [9] P. Krekora, Q. Su, and R. Grobe, "Critique of the Wigner tunneling speed and a proposed alternative," *Physical Review A*, vol. 64, no. 2, article 022105, 2001.
- [10] L. J. Zipp, A. Natan, and P. H. Bucksbaum, "Probing electron delays in above-threshold ionization," *Optica*, vol. 1, no. 6, pp. 361–364, 2014.
- [11] X. Gong, C. Lin, F. He et al., "Energy-resolved ultrashort delays of photoelectron emission clocked by orthogonal two-color laser fields," *Physical Review Letters*, vol. 118, no. 14, article 143203, 2017.
- [12] X. Song, G. Shi, G. Zhang et al., "Attosecond time delay of retrapped resonant ionization," *Physical Review Letters*, vol. 121, no. 10, article 103201, 2018.
- [13] P. Ge, M. Han, M. Liu, Q. Gong, and Y. Liu, "Probing time delays and coherent imaging of multiphoton resonant ionization," *Physical Review A*, vol. 98, no. 1, article 013409, 2018.
- [14] Y. Feng, M. Li, S. Luo et al., "Semiclassical analysis of photoelectron interference in a synthesized two-color laser pulse," *Physical Review A*, vol. 100, no. 6, article 063411, 2019.
- [15] M. Han, P. Ge, Y. Shao et al., "Revealing the sub-barrier phase using a spatiotemporal interferometer with orthogonal two-color laser fields of comparable intensity," *Physical Review Letters*, vol. 119, no. 7, article 073201, 2017.
- [16] M. Han, P. Ge, Y. Shao, Q. Gong, and Y. Liu, "Attoclock photoelectron interferometry with two-color corotating circular fields to probe the phase and the amplitude of emitting wave packets," *Physical Review Letters*, vol. 120, no. 7, article 073202, 2018.
- [17] P. Ge, M. Han, Y. Deng, Q. Gong, and Y. Liu, "Universal description of the attoclock with two-color corotating circular fields," *Physical Review Letters*, vol. 122, no. 1, p. 013201, 2019.
- [18] S. Eckart, "Holographic angular streaking of electrons and the Wigner time delay," *Physical Review Research*, vol. 2, no. 3, article 033248, 2020.
- [19] D. Trabert, S. Brennecke, K. Fehre et al., "Angular dependence of the Wigner time delay upon tunnel ionization of H_2 ," *Nature Communications*, vol. 12, no. 1, p. 1697, 2021.
- [20] P. Ge, Y. Fang, Z. Guo et al., "Probing the spin-orbit time delay of multiphoton ionization of Kr by bicircular fields," *Physical Review Letters*, vol. 126, no. 22, article 223001, 2021.
- [21] Z. Guo, Y. Fang, P. Ge et al., "Probing tunneling dynamics of dissociative H_2 molecules using two-color bicircularly polarized fields," *Physical Review A*, vol. 104, no. 5, article L051101, 2021.
- [22] M. Meckel, A. Staudte, S. Patchkovskii et al., "Signatures of the continuum electron phase in molecular strong-field photoelectron holography," *Nature Physics*, vol. 10, no. 8, pp. 594–600, 2014.

- [23] M. M. Liu, M. Li, C. Wu, Q. Gong, A. Staudte, and Y. Liu, "Phase structure of strong-field tunneling wave packets from molecules," *Physical Review Letters*, vol. 116, no. 16, article 163004, 2016.
- [24] A. Khan, D. Trabert, S. Eckart, M. Kunitski, T. Jahnke, and R. Dörner, "Orientation-dependent dissociative ionization of H_2 in strong elliptical laser fields: modification of the release time through molecular orientation," *Physical Review A*, vol. 101, no. 2, article 023409, 2020.
- [25] J. Yan, W. Xie, M. Li et al., "Photoelectron ionization time of aligned molecules clocked by attosecond angular streaking," *Physical Review A*, vol. 102, no. 1, article 013117, 2020.
- [26] A. Trabattoni, J. Wiese, U. De Giovannini et al., "Setting the photoelectron clock through molecular alignment," *Nature Communications*, vol. 11, no. 1, article 2546, 2020.
- [27] J. Ullrich, R. Moshhammer, A. Dorn, R. Dörner, L. P. H. Schmidt, and H. Schmidt-Böcking, "Recoil-ion and electron momentum spectroscopy: reaction-microscopes," *Reports on Progress in Physics*, vol. 66, no. 9, pp. 1463–1545, 2003.
- [28] I. Znakovskaya, P. von den Hoff, S. Zherebtsov et al., "Attosecond control of electron dynamics in carbon monoxide," *Physical Review Letters*, vol. 103, no. 10, article 103002, 2009.
- [29] R. N. Zare, "Dissociation of H_2^+ by electron impact: calculated angular distribution," *The Journal of Chemical Physics*, vol. 47, no. 1, pp. 204–215, 1967.
- [30] R. M. Wood, Q. Zheng, A. K. Edwards, and M. A. Mangan, "Limitations of the axial recoil approximation in measurements of molecular dissociation," *Review of Scientific Instruments*, vol. 68, no. 3, pp. 1382–1386, 1997.
- [31] M. Peters, T. T. Nguyen-Dang, E. Charron, A. Keller, and O. Atabek, "Laser-induced electron diffraction: a tool for molecular orbital imaging," *Physical Review A*, vol. 85, no. 5, article 053417, 2012.
- [32] M. D. Feit, J. A. Fleck Jr., and A. Steiger, "Solution of the Schrödinger equation by a spectral method," *Journal of Computational Physics*, vol. 47, no. 3, pp. 412–433, 1982.
- [33] E. Hasović, M. Busuladžić, W. Becker, and D. B. Milošević, "Dressed-bound-state molecular strong-field approximation: application to above-threshold ionization of heteronuclear diatomic molecules," *Physical Review A*, vol. 84, no. 6, article 063418, 2011.
- [34] M. Liu and Y. Liu, "Semiclassical models for strong-field tunneling ionization of molecules," *Journal of Physics B: Atomic, Molecular and Optical Physics*, vol. 50, no. 10, article 105602, 2017.
- [35] M. Li, M. Liu, J. Geng et al., "Experimental verification of the nonadiabatic effect in strong-field ionization with elliptical polarization," *Physical Review A*, vol. 95, no. 5, article 053435, 2017.
- [36] W. M. Huo, "Electronic structure of CO and BF," *The Journal of Chemical Physics*, vol. 43, no. 2, pp. 624–647, 1965.
- [37] P. E. Cade and W. M. Huo, "Hartree-Fock-Roothaan wavefunctions for diatomic molecules," *Atomic Data and Nuclear Data Tables*, vol. 15, no. 1, pp. 1–39, 1975.
- [38] J. Wu, L. P. H. Schmidt, M. Kunitski et al., "Multiorbital tunneling ionization of the CO molecule," *Physical Review Letters*, vol. 108, no. 18, article 183001, 2012.
- [39] D. B. Milošević, "Strong-field approximation for ionization of a diatomic molecule by a strong laser field," *Physical Review A*, vol. 74, no. 6, article 063404, 2006.
- [40] M. Busuladžić, A. Gazibegović-Busuladžić, D. B. Milošević, and W. Becker, "Strong-field approximation for ionization of a diatomic molecule by a strong laser field. II. The role of electron rescattering off the molecular centers," *Physical Review A*, vol. 78, no. 3, article 033412, 2008.
- [41] W. Becker, F. Grasbon, R. Kopold, D. B. Milošević, G. G. Paulus, and H. Walther, "Above-threshold ionization: from classical features to quantum effects," *Advances in Atomic, Molecular, and Optical Physics*, vol. 48, pp. 35–98, 2002.
- [42] J. Wiese, J. Onvlee, S. Trippel, and J. Küpper, "Strong-field ionization of complex molecules," *Physical Review Research*, vol. 3, no. 1, article 013089, 2021.